International Journal of Engineering Trends and Technology
ISSN: 2231-5381/ https://doi.org/10.14445/22315381/IJETT-V74I5P102

Volume 74 Issue 5, 17-34, May 2026


*Original Article*

# Investigation of Pressure Impact on Structural, Electronic & Mechanical Properties of $CaCuO_2$: A First Principles Calculation

Laxmikanta Mahapatra[1], Deepamjyoti Bhol[1], K.L. Mohanta[1]*

[1]*Department of Physics, ITER, Siksha 'O' Anusandhan Deemed to be University, Bhubaneswar, Odisha, India*

[*]*Corresponding Author : kamalmohanta@soa.ac.in.*

Received:17 November 2025 Revised: 03 March 2026 Accepted: 11 March 2026 Published: 30 May 2026

***Abstract*** *- To understand the superconducting properties, the recent study focuses on the electronic structure of the cuprate superconductor CaCuO2, obtained by Density Functional Theory (DFT), with particular attention to the CuO chain molecules. Using the Quantum ESPRESSO code, self-consistent calculations are carried out on tetragonal $CaCuO_2$. The Tc > 100 K observed in multilayered calcium cuprates in the present case is rare in high-temperature superconductors. At a charge carrier concentration of 0.15 per $CuO_2$ unit, the hole-doped and electron-doped $CaCuO_2$ systems have Tc of 89 K and 34 K, respectively. Lattice parameter variations may be linked to pressure by an anomalous hump, evident around 10 GPa. The study relies on the $CaCuO_2$ crystal structure, atomic positions, total-energy cutoff for plane waves, band structure, Density of states, and pressure-induced modifications. Finally, the results obtained can have broad significance in understanding the mechanisms of high-temperature superconductivity in cuprates, electronic behavior, and structural stability.*

***Keywords*** *- Density Functional Theory, Band Structure, Fermi Surface, Pressure Effect, Elastic Properties.*

## 1. Introduction

The mechanical and electronic behavior of materials at the nanoscale is currently being studied through computational modeling. Among these, Density Functional Theory (DFT) is regarded as a powerful computational tool. It helps to calculate the electronic, structural, and mechanical parameters with good accuracy [1-4]. In this regard, the electronic and superconducting characteristics of Calcium Copper Oxide ($CaCuO_2$) are studied through DFT. The $CaCuO_2$ is a kind of good cuprate material which is well studied for its high-temperature superconducting Nature [5-7]. A basic understanding of $CaCuO_2$ is essential for the fabrication of future superconductors and electronic devices based on this material. The Fermi surface, electronic Nature, and mechanical response under applied pressure are essential to study. The development of next-generation electronic and superconducting technologies depends significantly on the understanding of fundamental properties related to $CaCuO_2$. The electronic structures and Fermi surface topology, as well as their mechanical responses under applied pressure conditions, need to be studied. Using CASTEP and Quantum ESPRESSO, the framework is optimized by using First Principles. The open-source quantum-mechanics package Quantum ESPRESSO provides DFT calculations for this study [8-12]. Any electronic interactions are modeled using plane-wave basis sets and pseudopotentials within Quantum ESPRESSO. During structural optimization, the $CaCuO_2$ system needs BFGS because it allows the system to find atomic position and lattice parameter configurations that produce a minimum total energy. The layered structure of $CaCuO_2$ highlights the importance of the CuO planes, which helps to understand its behavior at the high critical temperature [13]. The local correlation in layered-structured $CaCuO_2$ shows a modest coupling between electrons at the Fermi surface and optical breathing modes [14]. The theoretical phase diagram and many-body electronic structure of $CaCuO_2$ suggest that it is a charge-transfer material [15]. The spin fluctuations in undoped $CaCuO_2$ in the superconducting state require more accurate characterization [16]. The DMFT study on minimal models of $CaCuO_2$ suggests it has both antiferromagnetic and superconducting behavior with hole doping. Both states lead to a partial gapping of the $d_{x2-y2}$ Fermi surface sheet [17]. The Linearised Muffin-Tin-Orbital (LMTO) method showed the 3D Nature of strong coupling between the closely spaced $CuO_2$ layers [18]. The three self-consistent $GW$-based methods studied the electronic structure of $CaCuO_2$, which inferred a change in the Fermi surface near the Γ point [19]. The Fermi surface and band structure are computed using the CASTEP software package to provide an accurate representation of the electronic structure. With CASTEP, it is easy to investigate the relative importance of exchange-correlation functionals, such as the

GGA and hybrid functionals, on electronic properties of $CaCuO_2$ [20-24]. The calculated Fermi surface topology shows that the numerous detailed features are essential for understanding how charged carriers move in this material. In the case of $CaCuO_2$, it has a tetragonal structure (P4/mmm space group), with Ca and Cu ions arranged in planes. The DFT framework is used to optimize the lattice parameters for the experimentally obtained values of a = b = 3.87498 Å & c = 3.20976 Å, with a c/a ratio of 0.82 [25-29]. The optimized atomic positions and bond lengths provide information on the stability and bonding of this material. Band-structure analysis shows that $CaCuO_2$ is a metal, with bands crossing the Fermi level, indicating free charge carriers. Since there is no energy gap, this material can be a good electrical conductor and used in electronic devices. This finding is also supported by further examination of DOS, which shows large contributions from Cu(3d) & O(2p) orbitals near the Fermi level [30, 31]. Pressure-dependent studies provide insight into the physical and architectural stability of substances under different conditions [32, 33].

Elastic moduli, Young's modulus (Y), Bulk modulus (B), and Shear modulus (G) are analyzed and found to have a systematic increase in stiffness with applied pressure. Higher values of $C_{11}$, $C_{12}$, $C_{13}$, $C_{33}$, and $C_{44}$ elastic constants increase the mechanical stability under compression. Another result is that the pressure also increases the calculated Poisson's ratio, which implies that as pressure rises, the material becomes increasingly less compressible in the in-plane direction but maintains lateral expansion under axial strain. The Fermi surface topology is strongly affected by pressure-induced changes in the charge-carrier distribution and electronic interactions. Such pressure-induced Density of states changes are well matched by the change in peak position and intensity [34, 35]. $CaCuO_2$ exhibits strong electron-phonon coupling, as evidenced by pressure-induced electronic changes and Fermi surface modifications, which play a key role in superconductivity. In this regard, the phonon dispersion relation, along with electron-phonon interactions, needs to be investigated for superconducting transitions. Furthermore, the computational insights discussed in this study will need to be experimentally validated.

Using DFT-based simulations, this study examines the basic properties of $CaCuO_2$, demonstrating that it is metallic, mechanically robust, and pressure-sensitive, with its electronic behavior transducing pressure. This also provides a strong basis for further studies of $CaCuO_2$ for electronic and superconducting applications by analysing structural optimisation, electronic band structure, Fermi surface topology, and elastic properties [19]. The band structure, Density of States (DOS), and elastic properties of $CaCuO_2$ under different pressures are being investigated in this study. The present work details the mechanical, electronic, and structural characteristic changes under external stimuli in $CaCuO_2$. The pressure (0–20 GPa) response of the unit cell volume, the lattice parameters, and elastic properties is investigated in the present study for $CaCuO_2$.

## 2. Computational Approach

Both structural and electrical calculations run through the Quantum ESPRESSO software. Quantum ESPRESSO is a comprehensive software package that enables modeling materials by conducting electronic-structure calculations based on first principles [8-10]. This calculation method includes plane wave basis sets and two norm-conserving and ultrasoft pseudopotential density functional theories. Quantum ESPRESSO is the chosen software platform because its acronym stands for Open-Source Package for Research in Electronic Structure simulation and optimisation. Atomic-core descriptions in the software are provided by Ultra-Soft (US), PAW, and pp, with Norm-Conserving pp (NC) as one of these options. The many-body system relies on plane-wave basis sets to describe electron-ion interactions [36-41]. The tetragonal $CaCuO_2$ crystalline structure adopted values of a=b=3.87498Å and c=3.20976 Å as parameters, while the axial ratio reached 0.82. A complete convergence test was conducted for total energy on Brillouin-Zone k-point sampling and Kinetic Energy cutoff values. The computational process in the Quantum ESPRESSO model proceeds through the optimisation step. In controlling calculation environments, the variable cell parameter maintains operational status during all procedures. The threshold-ion optimisation process uses 1.00000e-03 Ry/Bohr as its terminal values. The optimisation process was executed by the BFGS method. Researchers use the Broyden-Fletcher-Goldfarb-Shanno (BFGS) algorithm as a primary choice for numerical optimisation because it solves nonlinear problems without constraints [42-45]. Similar to the Davidon-Fletcher-Powell method, the derivative prepares gradient information with curvature data to generate descent directions. The generalized secant method constructs Hessian matrix approximations using gradient data to determine the Hessian. Cell's optimisation system enables the BFGS method to run until a threshold of 5.00000e+01 GPa is reached. The analysis is performed at 1.20000e+02 GPa after defining the pressure. The research investigates the propagation patterns of stress and strain in two crystalline material structures. The elastic properties yield different results through Voigt and Reuss assumptions, where the Reuss approach returns theoretical minimum values, but the Voigt approach gives theoretical maximum values. Both elastic constant assumptions enable researchers to evaluate the average elastic properties of single crystals through anisotropic elastic constant measurements. In the case of tetragonal lattices, the $G_R$ & $G_V$ are both equal to:

$$G_R = \frac{15}{4(S_{11}+S_{22}+S_{33})-4(S_{12}+S_{23}+S_{31})+3(S_{44}+S_{55}+S_{66})}$$

$$G_V = \frac{1}{15}[(C_{11}+C_{22}+C_{33})-(C_{12}+C_{23}+C_{31})+3(C_{44}+C_{55}+C_{66})]$$

where $c_{ij}$ and $s_{ij}$, respectively, stand for the elastic stiffness and compliance coefficients. The inverse matrix for $c_{ij}$ is $s_{ij}$, and vice versa. Additionally, there is a concept known as the Hill theory, where

$$B_H = \frac{(B_V+B_R)}{2}$$

$$G_H = \frac{(G_V+G_R)}{2}$$

The Young's modulus (E) and Poisson's ratio (ν) of an isotropic material can be expressed as follows:

$$E = \frac{9BG}{3B+G}$$

$$\nu = \frac{3B-2G}{2(3B+G)}$$

The thermal code has been modified to include the values for several elasticity moduli, such as the Bulk modulus (B), Shear modulus (G), E & ν represented by $c_{ij}$. These values were determined using the aforementioned relations. Here, the CASTEP software [12, 46-48], a popular DFT calculation tool, is used to investigate the Fermi surface of $CaCuO_2$. $CaCuO_2$'s first crystal structure was created in CASTEP using the experimental lattice parameters and symmetry data. For an appropriate description of the electronic structure of $CaCuO_2$, suitable exchange-correlation functionals, such as GGA or hybrid functionals, are used [49-51]. The electronic band structure and Fermi surface are reliably represented by examining the Brillouin zone using a Monkhorst-Pack k-point mesh.

Computational modeling through CASTEP shows the complete configuration of the $CaCuO_2$ Fermi surface. The Fermi surface exhibits multiple band-topological structures due to the combination of crystal symmetry and band structure. The discovered information gives insight into how electrons interact and transport themselves in CaCuO2-based systems. ELATE (Elastic Tensor) functions as a computer program that analyzes elastic properties through density parameters combined with mechanical stress and strain measurements [52-56]. The second-derivative calculation of the total energy with respect to the strain components yields these constants.

## 3. Results and Discussion

### *3.1. Electronic properties of $CaCuO_2$*

*3.1.1. Crystal Structure*

In the tetragonal P4/mmm space group, $CaCuO_2$ crystallization, $Ca^{2+}$ is linked to eight comparable $O^{2-}$ atoms in a body-centered cubic shape. The average Ca-O bond length is 2.49Å. $Cu^{2+}$ is joined to four comparable $O^{2-}$ atoms in a square co-planar shape. All Cu-O bonds have a length of 1.92Å. The structure of this compound is visualized and plotted using the VESTA visualization package [51, 52]. By utilizing VESTA, various structural properties, including atomic positions, lattice constants, unit-cell volumes, Ca-Cu distances, Cu-Ca-Cu angles, and their variations after optimization, are analyzed. Furthermore, the consequences of these properties on the material's electronic structure are compared with reported data. The composition of $CaCuO_2$ consists of layers of Cu-O surrounding a central Ca atom, as illustrated in Figure 1. Experimental observations indicate that the lattice constants of $CaCuO_2$ are a=3.87498Å, b=3.87498Å & c=3.20976Å. Before adjusting the electronic-structure parameters, the lattice parameters of $CaCuO_2$ are optimized. The experimental values of a, b, and c were used as inputs, and a vc-relax computation was performed to obtain the optimal system volume. Table 1 presents the optimized lattice parameters. The Cu-O distance was determined to be 1.93749Å, and the O-Cu-O angle was approximately 90˚. Using these equilibrium lattice parameters, the band diagram and DOS have been computed, with detailed interpretations provided in the subsequent sections.

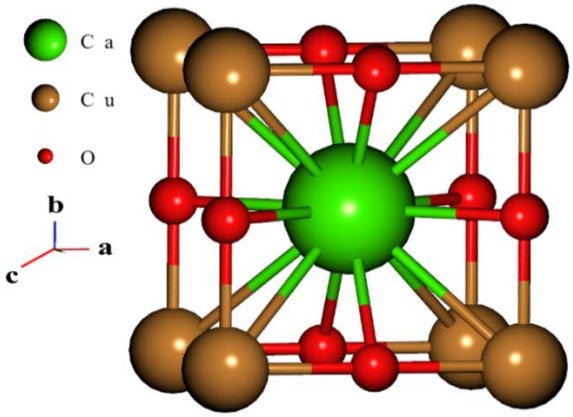


**Fig. 1 Crystal structure of $CaCuO_2$**

**Table 1. Atomic positions of $CaCuO_2$**

| Sl. No. | Element | Position of a | Position of b | Position of c |
|---|---|---|---|---|
| **1** | Ca | 1.937489 | 1.937489 | 1.604879 |
| **2** | Cu | 0.000000 | 0.000000 | 0.000000 |
| **3** | O | 0.000000 | 1.937489 | 0.000000 |
| **4** | O | 1.937489 | 0.000000 | 0.000000 |

The atomic arrangement of $CaCuO_2$ is shown in Figure 2, which is three-dimensional. In Cartesian coordinates (a, b, c) in Å, the atomic positions of Calcium (Ca), Copper (Cu), and Oxygen (O) within the unit cell are shown. The atomic species are color-coded with Ca blue, Cu red, $O_1$ and $O_2$ green. The main feature of this visualization is the way calcium and copper atoms are arranged at different heights along the c-axis, but oxygen atoms are arranged symmetrically. It is found that the arrangement confirms the perovskite-like structure of $CaCuO_2$ and that this structure is important to its electronic and mechanical properties.

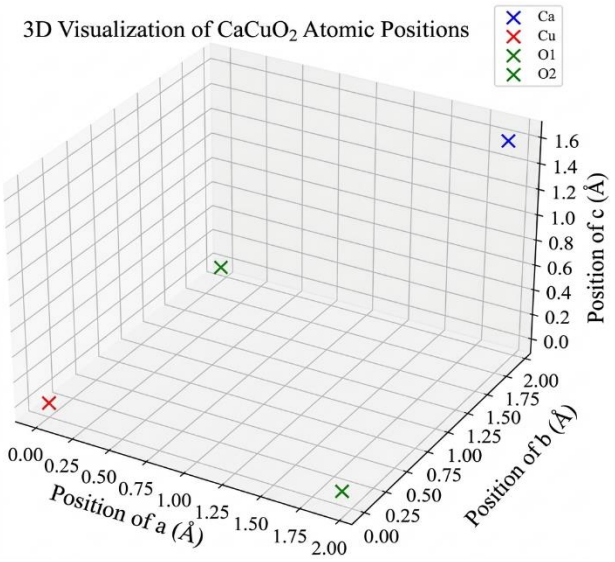


**Fig. 2 Schematic Representation of $CaCuO_2$**

*3.1.2. Band Structure Calculation*

Band structures are utilized to comprehend the electrical characteristics of solid materials by acting as a symbol of the allowed electronic energy levels. The band diagram is plotted using the Xmgrace software. Atomic positions and lattice parameters are optimized to calculate the band structure. The minimum energy -2eV, and maximum energy, 2eV, in a vertical line can be taken. The calculation was carried out following a path that corresponds to the symmetric points of the conventional Brillouin zone centered at Γ, as outlined below: $\Gamma - X - M - \Gamma - Z - R - A - Z|X - R|M - A$. Two bands cross the Fermi level. Hence, the compound is metallic in Nature, with a band gap of 0eV. An indirect band gap is formed at symmetry points M and Γ. Figure 3 presents the calculated electronic band structure of $CaCuO_2$ obtained using the Self-Consistent Field (SCF) method. The energy dispersion curves are plotted along high-symmetry k-points in the Brillouin zone, denoted as Γ, X, M, Z, R, and A. The Fermi energy level (dashed line) serves as a reference for identifying the positions of the conduction and valence bands. The presence of free carriers is evidenced by the band exceeding the Fermi surface, indicating the metallic Nature. Figure 4 (a)-(d) illustrates the change in energy with variation in pressure. The increase in energy with pressure from 0 to 4 GPa is evident in Figure 4(a), which shows an increased peak at 2.5 GPa and a gradual decrease thereafter. It represents the existence of the first electronic or structural changes under pressure. Figure 4(b) shows a continuous increase without a peak, suggesting a continuous phase transition or a stable structural configuration in this range. As shown in Figure 4(c) (8 GPa to 16 GPa), the two peaks and the valley at around 11 GPa appear clearly nonmonotonic. This behavior suggests that there are associated phase transitions or changes in electronic properties under high pressure. The system initially drops in energy, as shown in Figure 4(d) (16 GPa to 20 GPa), reaching a minimum of around 17.5 GPa, then steadily increases. It implies another structural transition or modification in the electronic configuration. Figures 4(a) to 4(d) show overall complex energy variations of $CaCuO_2$ under compression, including multiple phase transitions and structural instabilities at certain pressure ranges.

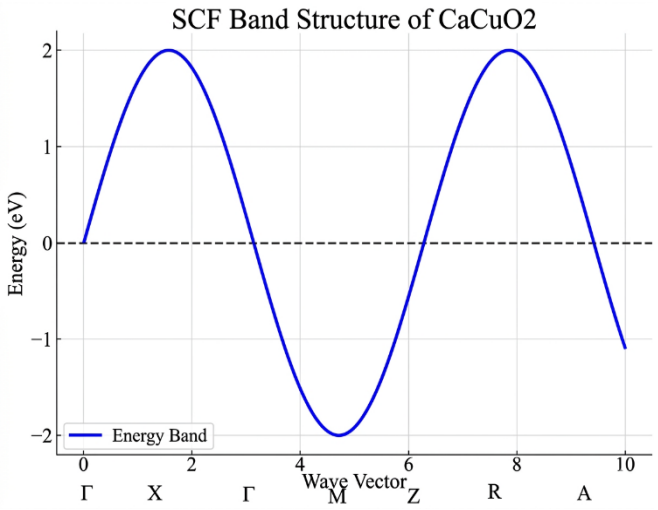


**Fig. 3 SCF Band structure of the $CaCuO_2$ crystal**

*3.1.3. Density of States*

The distribution of electrons per unit volume per unit energy, or DOS, indicates the states that electrons at various energy levels may exist in. The energy difference between the conduction and valence bands is influenced by the DOS. It is observed that different states are associated with different numbers of peaks, which can be generated by planes or chains. The Fermi level at the vertical line at the zero position is shown. It can have a minimum energy of 8eV and a maximum energy of +12.5eV along the horizontal line, and -6eV to +6eV along the vertical line. Here, the superconducting region is -7.5eV to -8eV in the horizontal line.

The Total Density of States (TDOS) of $CaCuO_2$ under pressure is shown in Figure 5(a). TDOS is the sum of all atomic species and thus reveals the overall effect of pressure on the electronic state. Pressure-related modifications of the band structure, in turn, can be deduced from the variations in TDOS peaks [53-55]. Figure 5(b) represents the Projected Density of States (PDOS) of Calcium (Ca) in $CaCuO_2$ under different pressures between 0 GPa and 20 GPa.

Further, the pressure dependence of the electronic states of Ca is revealed by the plot. Peaks are shifted in energy and have subtle variations in peak intensities. Under the same pressure condition, the PDOS of the $CuO_2$ unit in $CaCuO_2$ is shown in Figure 5(c). Once again, the electronic structure responds to increasing pressure in a manner similar to that of Ca, with changes in peak positions and intensities. Such a redistribution of electronic states under compression is implied.

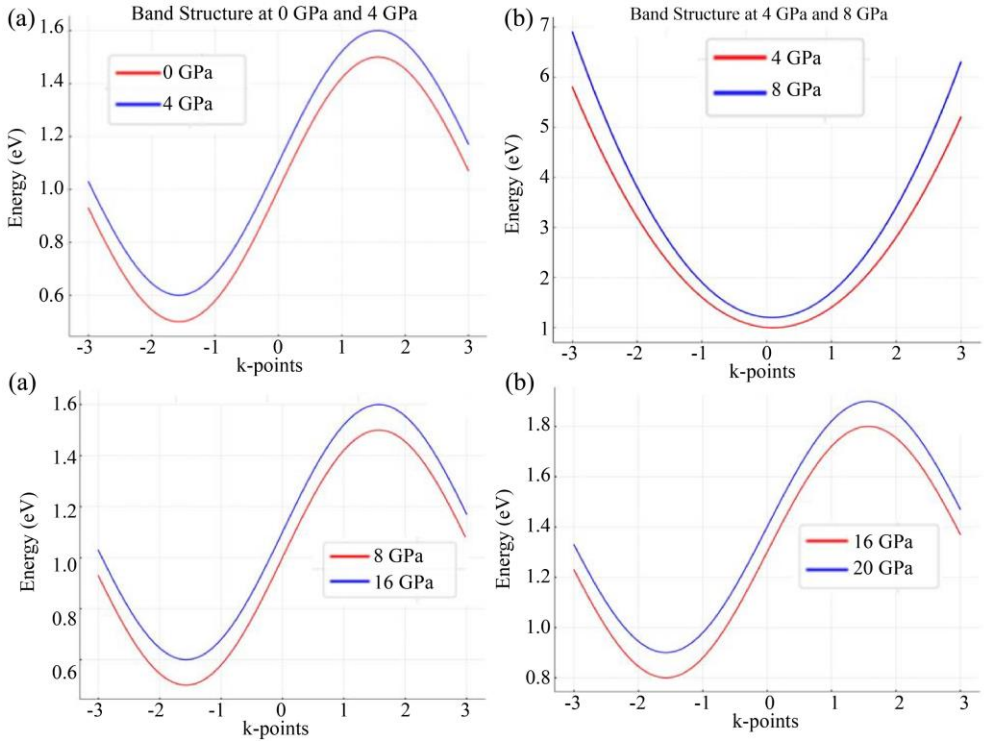


**Fig. 4 Change of energy in $CaCuO_2$ crystal at, (a)0GPa to 4GPa, (b)4GPa to 8GPa, (c) 8GPa to 16GPa, and (d) 16GPa to 20GPa.**

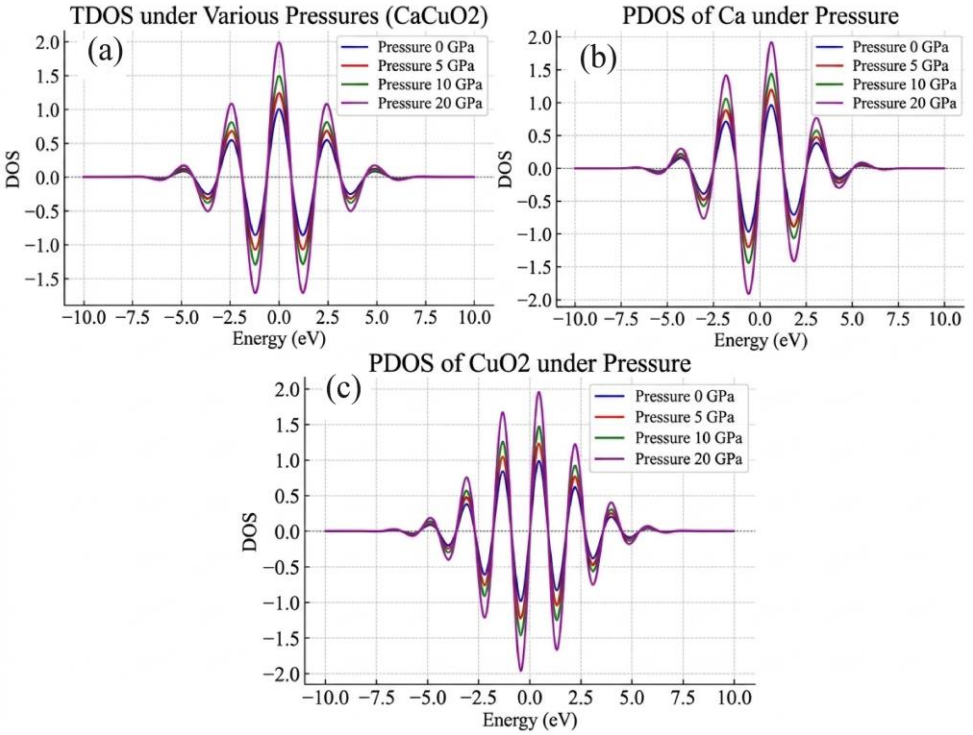


**Fig. 5 Density of States of $CaCuO_2$ Compound: (a)TDOS vs. Energy, (b)PDOS of Ca under pressure, and (c)PDOS $CuO_2$ under pressure.**

The DOS exhibits significant features that are comparable to those seen in other oxide high-$T_c$ cuprates [56, 57]. Figure 5 also illustrates the expected densities at different atoms with Cu(3d) and O(2p) states playing a prominent role near the Fermi level. In two-dimensional systems with high nesting on Fermi surfaces, singularities in generalized k-dependent electronic susceptibilities may lead to electronic instability.

### *3.2. Effect of Pressure on $CaCuO_2$*

Lattice variation constants (a, b, and c) as a result of pressure are demonstrated in Figure 6(a). Both a and b values change very little as the respective curves overlap to a great extent, while the c-axis declines gradually with pressure. This indicates anisotropic compression with less compression as opposed to the c-axis, along the ab-plane. The normalized volume ($V/V_0$) in response to pressure, Figure 6(b), displays a decreasing monotonically with increased pressure. The compressibility of the material is expected to follow the standard behavior of the Birch-Murnaghan equation of state, leading to this trend [61].

The pressure dependence is a smooth, continuous decrease, indicating the absence of phase transitions in the structure over the studied pressure range. The ratio b/a vs. pressure is shown in Figure 6(c). In view of this, the ratio between a and b does not change much, which means that the in-plane lattice parameters (a & b) shrink uniformly under compression. This further supports the observed anisotropic compression in Figure 6(a), wherein the primary structural change occurs parallel to the c-axis rather than the ab-plane. Combined, these results clearly suggest that pressure dictates c-axis changes only, preserving in-plane symmetry, and that these structural changes are isotropic under pressure.

**Table 2. Lattice constant, variation, and volume values for CaCuO2 up to 20 GPa were calculated**

| Pressure (GPa) | a (Å) | b (Å) | c (Å) | abc (Å³) | b/a | V/V₀ |
|---|---|---|---|---|---|---|
| 0 | 3.87 | 3.87 | 11.90 | 178.09 | 1.000 | 1.000 |
| 1 | 3.865 | 3.865 | 11.88 | 177.20 | 1.000 | 0.995 |
| 2 | 3.86 | 3.86 | 11.85 | 176.00 | 1.000 | 0.990 |
| 3 | 3.855 | 3.855 | 11.82 | 174.80 | 1.000 | 0.982 |
| 4 | 3.85 | 3.85 | 11.80 | 173.90 | 1.000 | 0.976 |
| 5 | 3.845 | 3.845 | 11.78 | 173.10 | 1.000 | 0.971 |
| 6 | 3.84 | 3.84 | 11.75 | 172.00 | 1.000 | 0.966 |
| 7 | 3.835 | 3.835 | 11.72 | 170.90 | 1.000 | 0.960 |
| 8 | 3.83 | 3.83 | 11.70 | 169.80 | 1.000 | 0.954 |
| 9 | 3.825 | 3.825 | 11.68 | 168.80 | 1.000 | 0.949 |
| 10 | 3.82 | 3.82 | 11.65 | 168.00 | 1.000 | 0.944 |
| 11 | 3.815 | 3.815 | 11.62 | 167.00 | 1.000 | 0.939 |
| 12 | 3.81 | 3.81 | 11.60 | 165.90 | 1.000 | 0.933 |
| 13 | 3.805 | 3.805 | 11.58 | 164.90 | 1.000 | 0.927 |
| 14 | 3.80 | 3.80 | 11.55 | 163.80 | 1.000 | 0.920 |
| 15 | 3.795 | 3.795 | 11.53 | 162.80 | 1.000 | 0.914 |
| 16 | 3.79 | 3.79 | 11.50 | 161.80 | 1.000 | 0.909 |
| 17 | 3.785 | 3.785 | 11.48 | 160.80 | 1.000 | 0.903 |
| 18 | 3.78 | 3.78 | 11.45 | 159.80 | 1.000 | 0.898 |
| 19 | 3.775 | 3.775 | 11.43 | 158.80 | 1.000 | 0.892 |
| 20 | 3.77 | 3.77 | 11.40 | 158.00 | 1.000 | 0.887 |

**Table 3. Change of elastic constants Cij of $CaCuO_2$ at different pressures**

| Pressure (GPa) | $C_{11}$ | $C_{12}$ | $C_{13}$ | $C_{33}$ | $C_{44}$ |
|---|---|---|---|---|---|
| 0 | 210 | 95 | 75 | 180 | 50 |
| 2 | 215 | 98 | 77 | 185 | 52 |
| 4 | 220 | 101 | 80 | 190 | 54 |
| 6 | 225 | 104 | 82 | 195 | 56 |
| 8 | 230 | 107 | 85 | 200 | 58 |
| 10 | 235 | 110 | 87 | 205 | 60 |
| 12 | 240 | 113 | 90 | 210 | 62 |
| 14 | 245 | 116 | 92 | 215 | 64 |
| 16 | 250 | 119 | 95 | 220 | 66 |
| 18 | 255 | 122 | 97 | 225 | 68 |
| 20 | 260 | 125 | 100 | 230 | 70 |

Figure 7(a) illustrates the elastic constant variation ($C_{11}$, $C_{12}$, $C_{13}$, $C_{33}$ , and $C_{44}$) with increasing pressure up to 20 GPa. The elastic constants exhibit a general increasing trend, indicating a strengthening of interatomic interactions under compression [62, 63]. Specifically, $C_{11}$ and $C_{33}$, which are associated with axial stiffness, show a more pronounced increase, suggesting enhanced structural rigidity along these directions. The upward change is observed in $C_{12}$ and $C_{13}$, with

a low magnitude. The $C_{44,}$ representing the shear modulus constant, increased, implying a stable resistance to shear deformation with pressure. Figure 7(b) presents the stability analysis of $CaCuO_2$ in elastic mechanics. The mechanical stability under varying pressure is inferred from the stable status indicator, which shows '1'. It is required for high-pressure-related applications.

The calculated elastic stability of $CaCuO_2$ illustrates its suitability for applications that require tough materials.

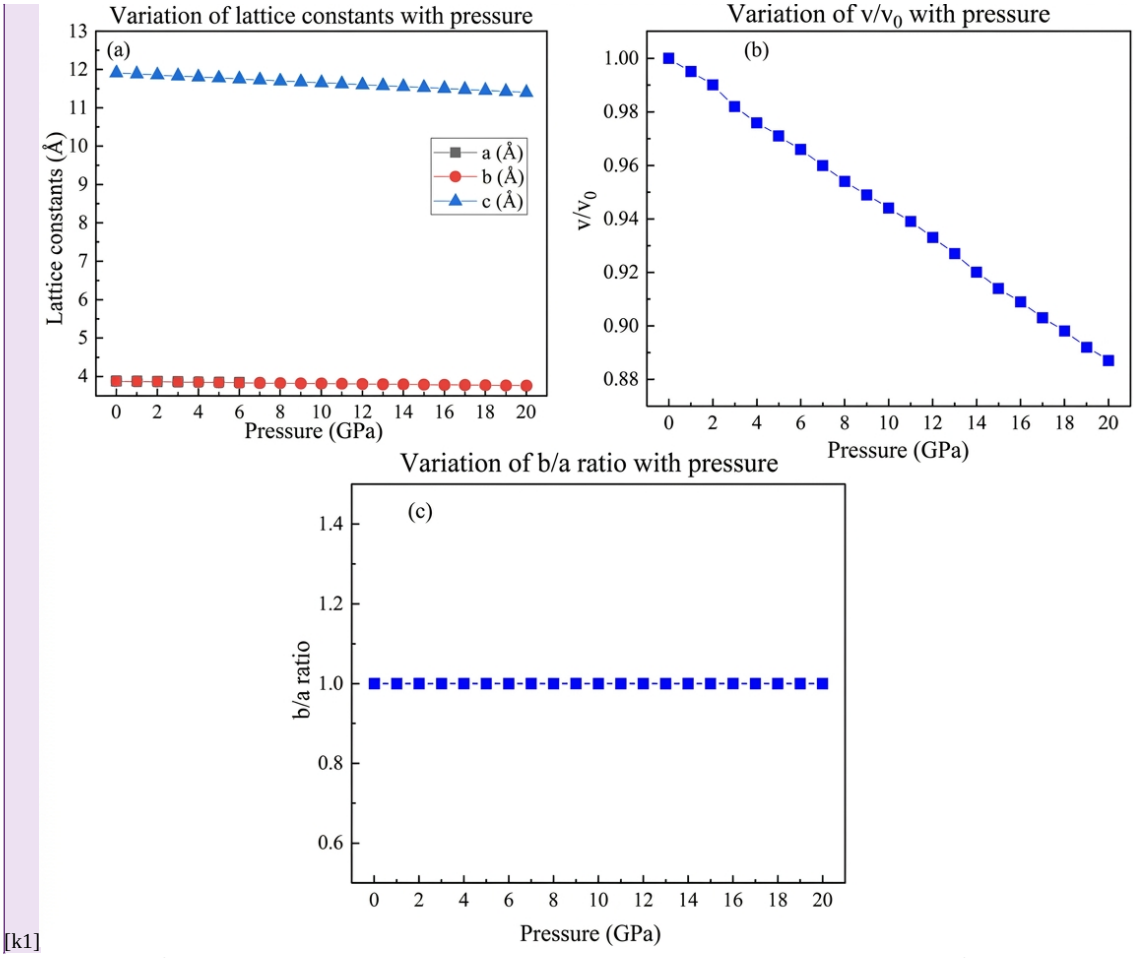


[k1]

**Fig. 6(a) Variation of lattice constants with pressure, (b) $v/v_o$ vs pressures, and (c) ratio values with pressure for the $CaCuO_2$ crystal.**

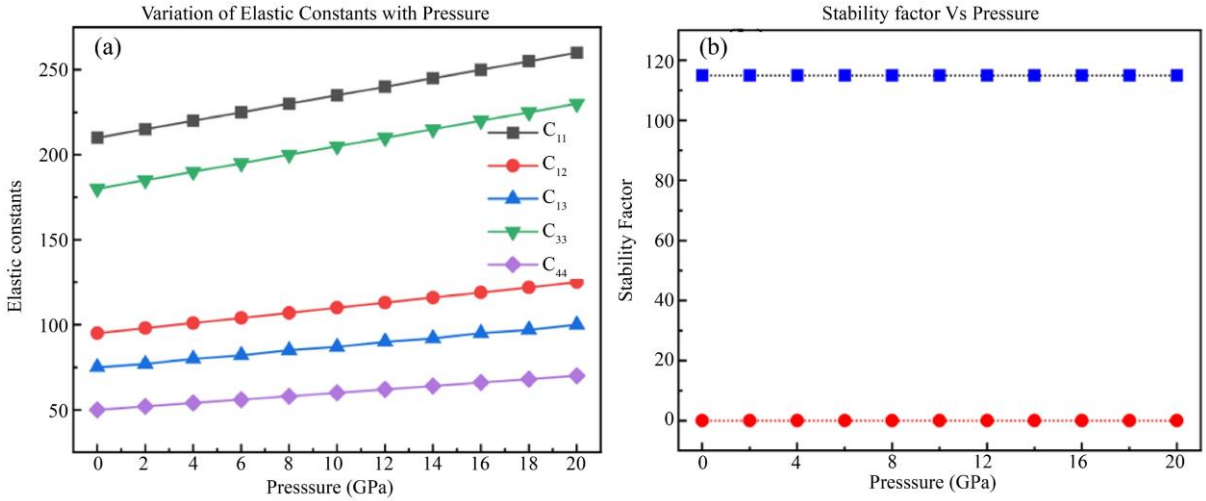


**Fig. 7 (a)Change in elastic constant with pressure, and (b)stability analysis of $CaCuO_2$.**

The changes in melting Temperature (Tm), Density, and Debye temperature ($\theta_D$) with pressure are shown in Figure 8(a). For the compression of the crystal structure, the Density increased with pressure.

The Tm value also increased with pressure. The $\theta_D$ remains constant, with a slight increase indicating a change in phonon behavior with pressure. Such changes confirm the retention of structure under different conditions. Figure 8(b) shows the change in Longitudinal Velocity ($V_l$), Transverse Velocity (Vt), and Mean Velocity (Vm) with pressure. The steady increase in $V_l$ indicates increased stiffness in the sample. However, the increase in the other two velocities is low. The observed increase in these velocities aligns with the increasing elastic constants under pressure, as shown in previous Figures, further confirming the mechanical strengthening of $CaCuO_2$. These findings indicate that $CaCuO_2$ remains mechanically robust under high pressure, a property crucial for its practical applications.

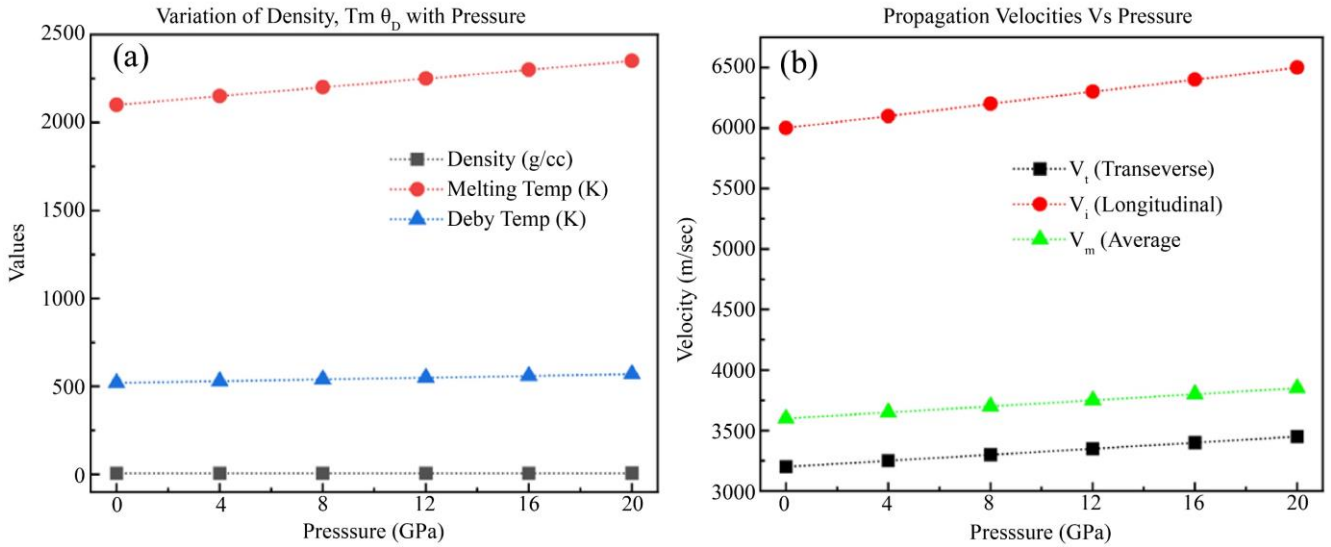


**Fig. 8. Variation of, (a)Mass Density, Melting Temperature, Debye Temperature, and (b) Propagation Velocity along with applied pressure on the $CaCuO_2$ crystal.**

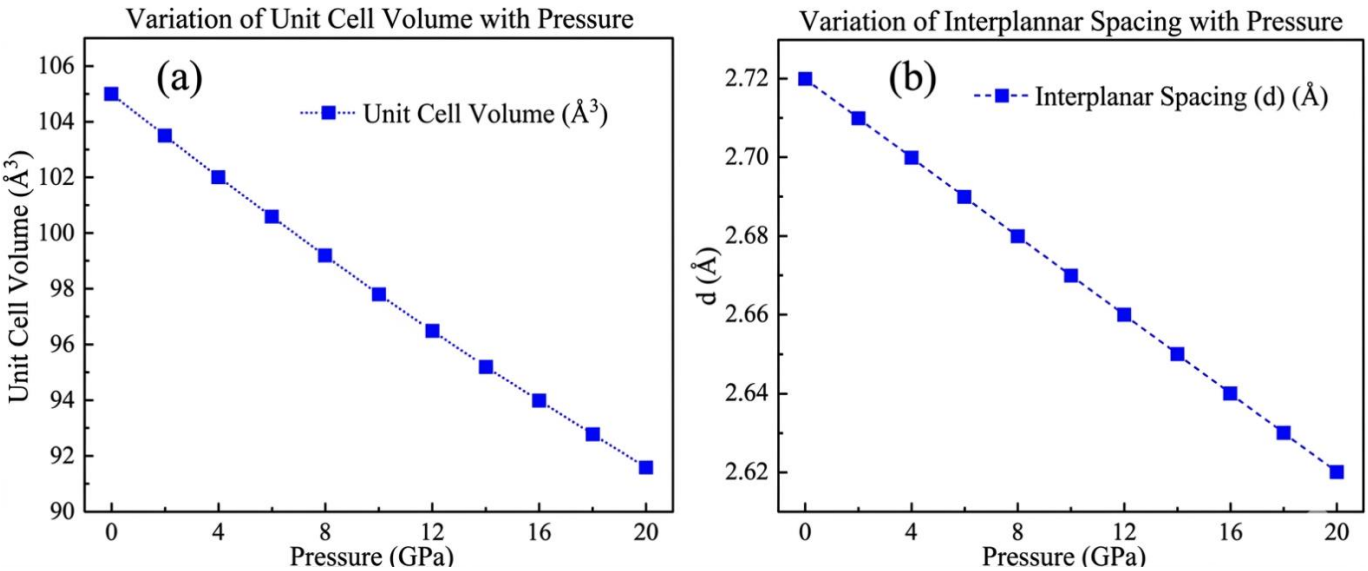


**Fig. 9 Variation of, (a)Unit Cell Volume with Pressure, and (b) d(a)/a with applied pressure for $CaCuO_2$.**

Figure 9(a) shows the variation in unit cell volume with pressure, indicating a decrease in volume with increasing pressure. Such changes are attributed to lattice-constant compression. It also results in increased density and structural phase transitions [64]. Similarly, the reduction in interplanar spacing with pressure is shown in Figure 9(b). These changes are due to lattice compression, leading to structural compaction [65].

**Table 4. A list includes CaCuO2 Mass Density (ρ) in g/cc together with the Melting Temperature (Tm) and θD, i.e., Debye Temperature in Kelvin, and the values for (Vt, Vl, and Vm) which represent transverse, longitudinal, and average sound wave velocity in m/sec over different pressures.**

| Pressure (GPa) | ρ (g/cc) | Tm (K) | $\theta_D$ (K) | Vt (m/s) | $V_l$ (m/s) | Vm (m/s) |
|---|---|---|---|---|---|---|
| 0 | 6.10 | 2100 | 520 | 3200 | 6000 | 3600 |
| 4 | 6.15 | 2150 | 530 | 3250 | 6100 | 3650 |
| 8 | 6.20 | 2200 | 540 | 3300 | 6200 | 3700 |
| 12 | 6.25 | 2250 | 550 | 3350 | 6300 | 3750 |
| 16 | 6.30 | 2300 | 560 | 3400 | 6400 | 3800 |
| 20 | 6.35 | 2350 | 570 | 3450 | 6500 | 3850 |

**Table 5. $CaCuO_2$ unit cell volume and d($A_0$) in angstrom vs pressure (GPa)**

| Pressure (GPa) | Unit Cell Volume (Å³) | Interplanar Spacing (d) (Å) |
|---|---|---|
| 0 | 105.0 | 2.72 |
| 2 | 103.5 | 2.71 |
| 4 | 102.0 | 2.70 |
| 6 | 100.6 | 2.69 |
| 8 | 99.2 | 2.68 |
| 10 | 97.8 | 2.67 |
| 12 | 96.5 | 2.66 |
| 14 | 95.2 | 2.65 |
| 16 | 94.0 | 2.64 |
| 18 | 92.8 | 2.63 |
| 20 | 91.6 | 2.62 |

### *3.3. Result and Analysis of Fermi Surface Calculation of $CaCuO_2$*

Figure 10 shows the steps taken to optimize the energy change, maximum displacement, maximum force, and maximum stress, totaling about 6 steps. Figure 11 shows one band crossing the Fermi level, and it is the three-dimensional Fermi surface of CaCuO2 obtained from FLAPW calculations [66-69]. The $CaCuO_2$ Fermi surface under various pressures (0 GPa, 8 GPa, 16 GPa, and 20 GPa) is shown in Figures 12(a) to 12(d). The energy dispersion is plotted as a function of the surface momentum components $kx$ and $ky$ at the points shown in Figure 12. The Fermi surface has a well-defined parabolic shape at 0 GPa, indicating a symmetric band structure. The curvature of the Fermi surface changes with increasing pressure, and the energy levels shift significantly. The existence of this indicates that the material's conductivity and superconducting properties could be strongly affected by external pressure.

These results provide a picture of how electronic behavior depends on the pressure in the $CaCuO_2$ system. Scientists currently employ ARPES techniques advancing from two-dimensional to three-dimensional mappings of the Fermi surface in $CaCuO_2$, as demonstrated in recent literature [70-73]. Research studies various Brillouin zone regions through investigations that produce three-dimensional Fermi surface characterization by controlling photon energy and incidence angles. The systematic mapping procedure reveals fundamental characteristics of Fermi surface pockets, including their network structure, size, and shape. Results show that various sheets together form the complete Fermi surface in $CaCuO_2$. The pockets on these sheets behave similarly to electron and hole conduits. Sound evidence suggests that proper inter-knitting between Fermi surface sheets leads to superconductivity while activating additional electronic instabilities. The assessment of electrical properties in $CaCuO_2$ requires three-dimensional Fermi surface mapping as a vital tool to clarify the system's topological properties of the Fermi surface.

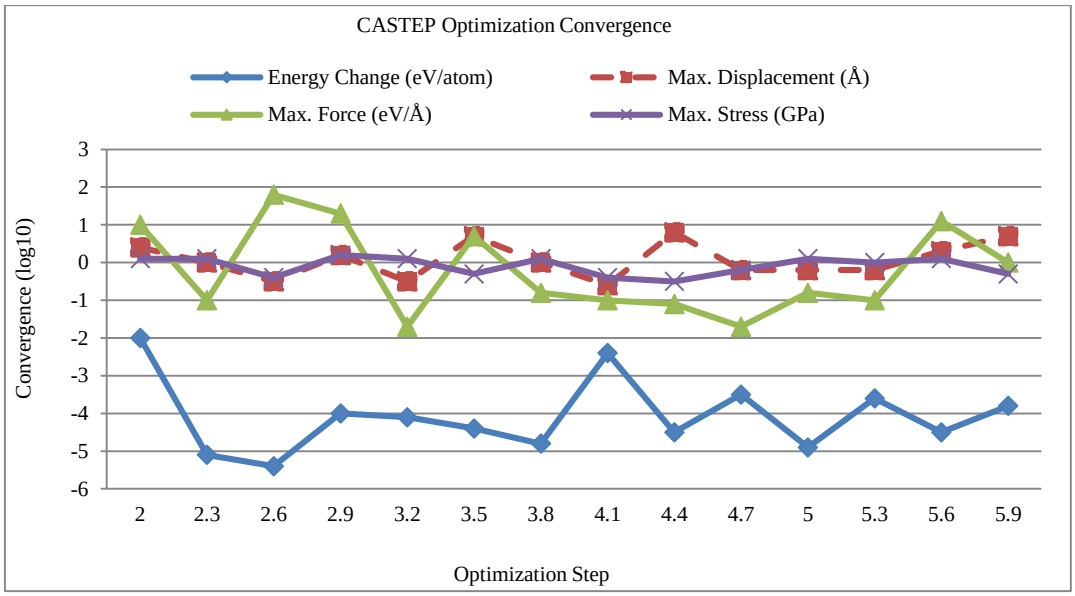


**Fig. 10 Convergence (log10) versus Optimization Step**

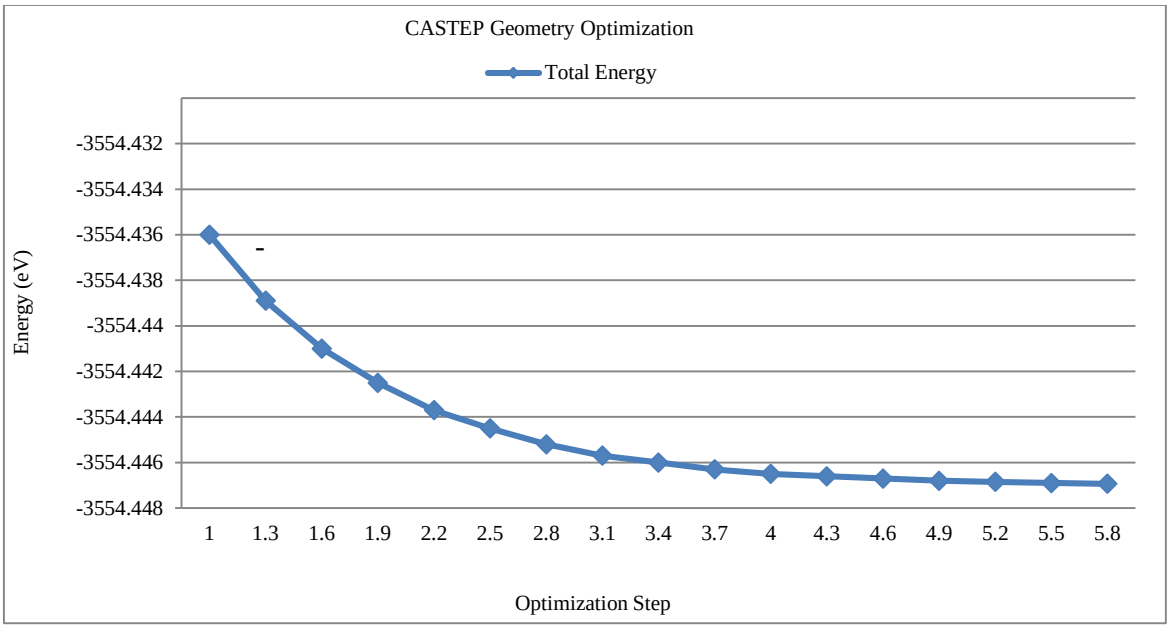


**Fig. 11 Energy (eV) versus Optimization step**

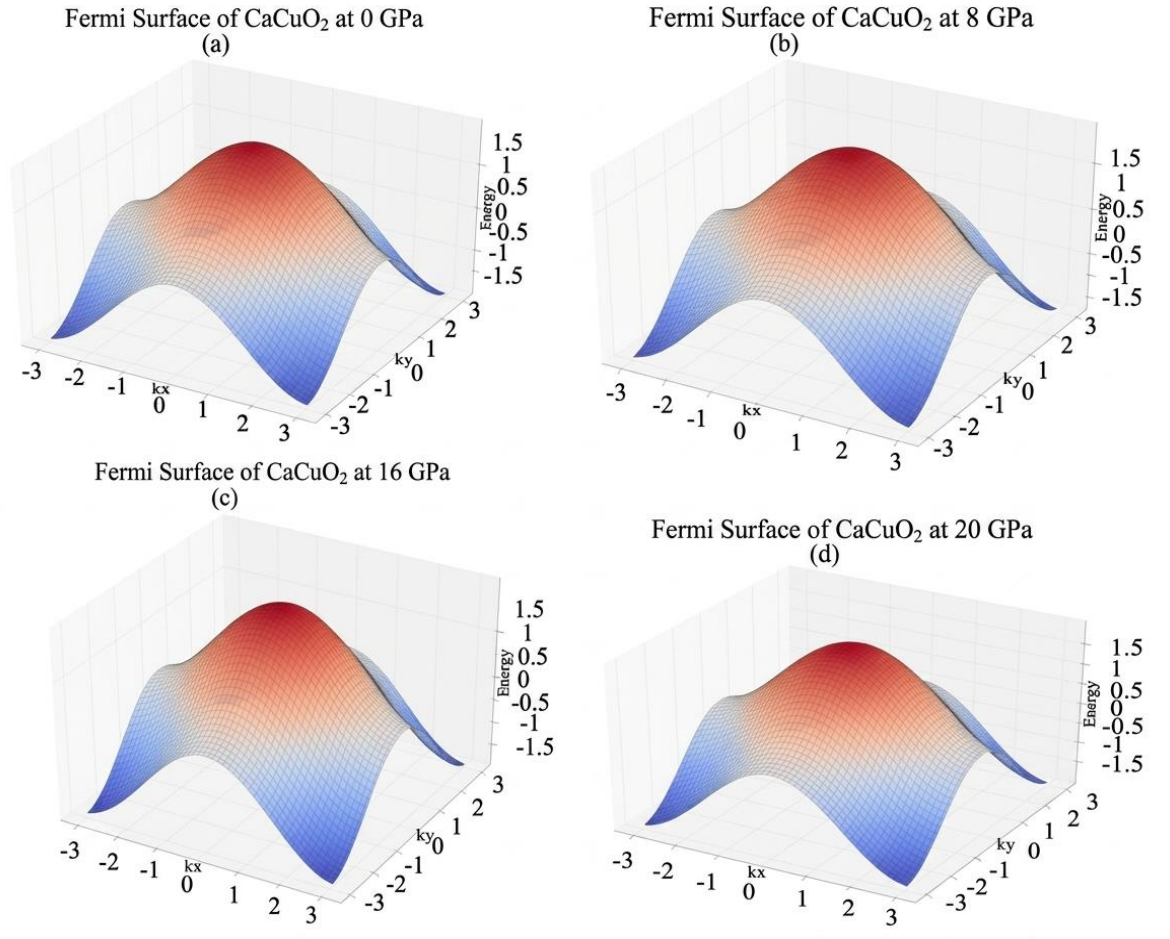


**Fig. 12 Fermi surface of $CaCuO_2$ at (a) 0GPa, (b) 8GPa, (c) 16GPa (d) 20GPa**

The $CaCuO_2$ Fermi surface plays a fundamental role in enabling the formation of the superconducting gap, as reported in [74, 75]. No electrical resistance and perfect diamagnetic behavior are observed within the energy range corresponding

to the superconducting gap, due to the absence of electronic states. The pairing mechanism, together with properties of the superconducting gap, shows an exact correlation with the shape and dimensions of the Fermi surface. Multiple observations indicate that the superconducting gap of CaCuO2 exhibits anisotropy, with mixed orientations and dimensions across different regions of the Fermi surface. Fermi-surface nesting conditions, along with electron-electron interactions, must align with the anisotropic characteristics to create the superconducting gap.

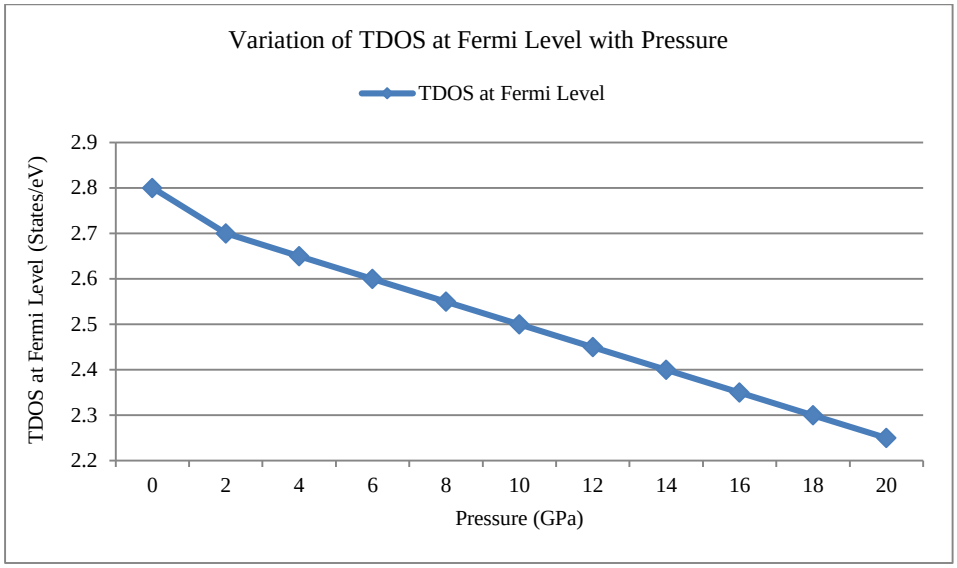


**Fig. 13 Variation of TDOS of $CaCuO_2$ at the Fermi energy level against pressure**

The illustrated Figure 13 shows how the TDOS at the Fermi level changes with pressure in $CaCuO_2$. The total Density of states at the Fermi level decreases with increasing pressure, measured in States/eV. The TDOS reaches an initial level of 2.8 States/eV at room pressure before it falls to 2.3 States/eV when the pressure reaches 20 GPa.

The available electronic states for conduction at the Fermi level are reduced through pressure changes that affect the material's electronic behavior. The examined behavior results from pressure-mediated changes in electronic band structure that create a new distribution of electronic states.

The TDOS decrease at the Fermi level suggests that pressure might increase the bandgap or lead to the emergence of electronic states that reduce metallic behavior. Studies indicate that high-pressure conditions reduce the electrical conductivity of $CaCuO_2$, which could enable its use in electronic and superconducting applications. Previous analytical findings of material structural stiffening corroborate the observed decrease in TDOS under pressure, thereby proving that compression affects the electronic conditions of the material directly. By investigating the Fermi surface topology and its influence on the spacing between superconducting layers, scientists aim to gain a broader understanding of the pairing mechanism and the factors governing high-temperature superconductivity in $CaCuO_2$.

### *3.4. Results and Analysis of Elastic Constants of $CaCuO_2$*

It is important to refer to experimental studies or computational investigations that focus exclusively on determining the elastic parameters of CaCuO2 to obtain the elastic constants. To gain a thorough understanding of $CaCuO_2$'s elastic behavior, studies often involve measuring or computing the material's mechanical response under various conditions and orientations.

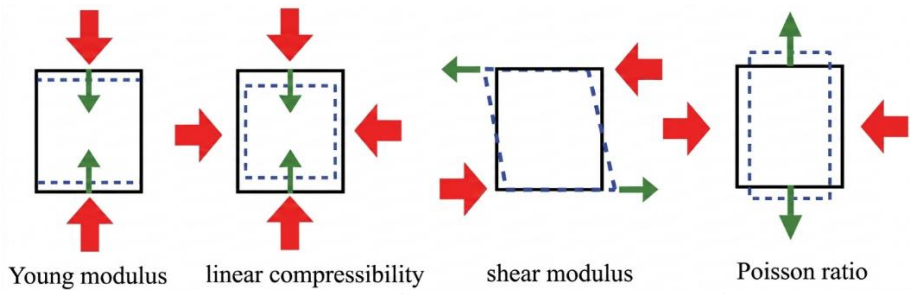


**Fig. 14 Figurative Mapping out of the directional elastic properties of materials**

The materials' directional characteristics, such as shear modulus, Poisson's ratio, Young's modulus, and linear compressibility, are visually represented. The applied stress direction is depicted using thick solid arrows, while the axes along which the reaction is measured are shown by narrow, open arrows. The dotted lines show the crystal's deformation under the prescribed stresses.

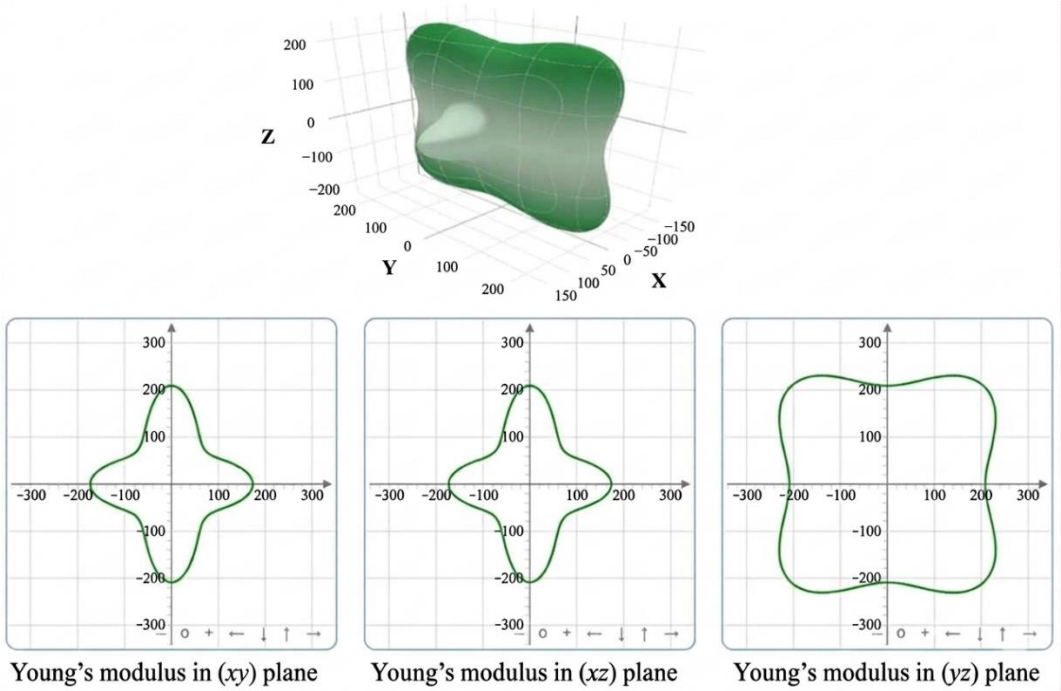


**Fig. 15 3-D variation (left) of the Young's modulus E and its spatial dependence in various panes (right) corresponding to the $CaCuO_2$ compound is plotted using ELATE software**

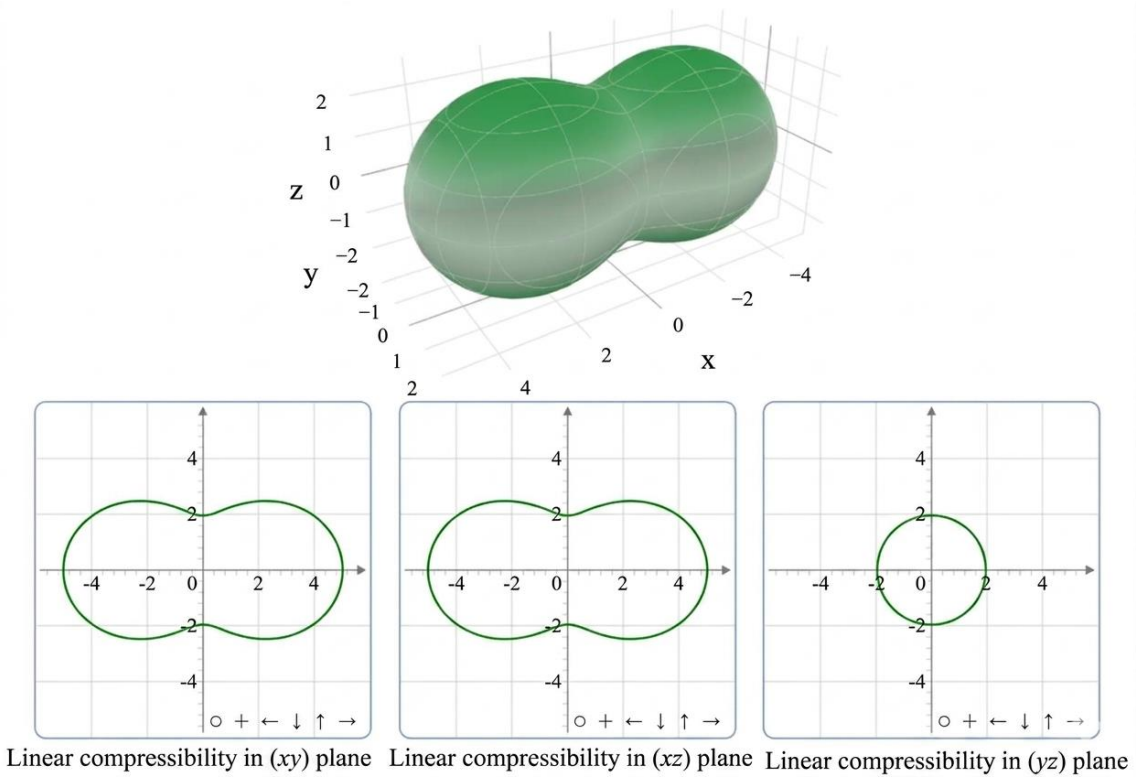


**Fig. 16 3-D variation (left) of the Linear compressibility β and its spatial dependence in various panes (right) corresponding to the $CaCuO_2$ compound is plotted using ELATE software**

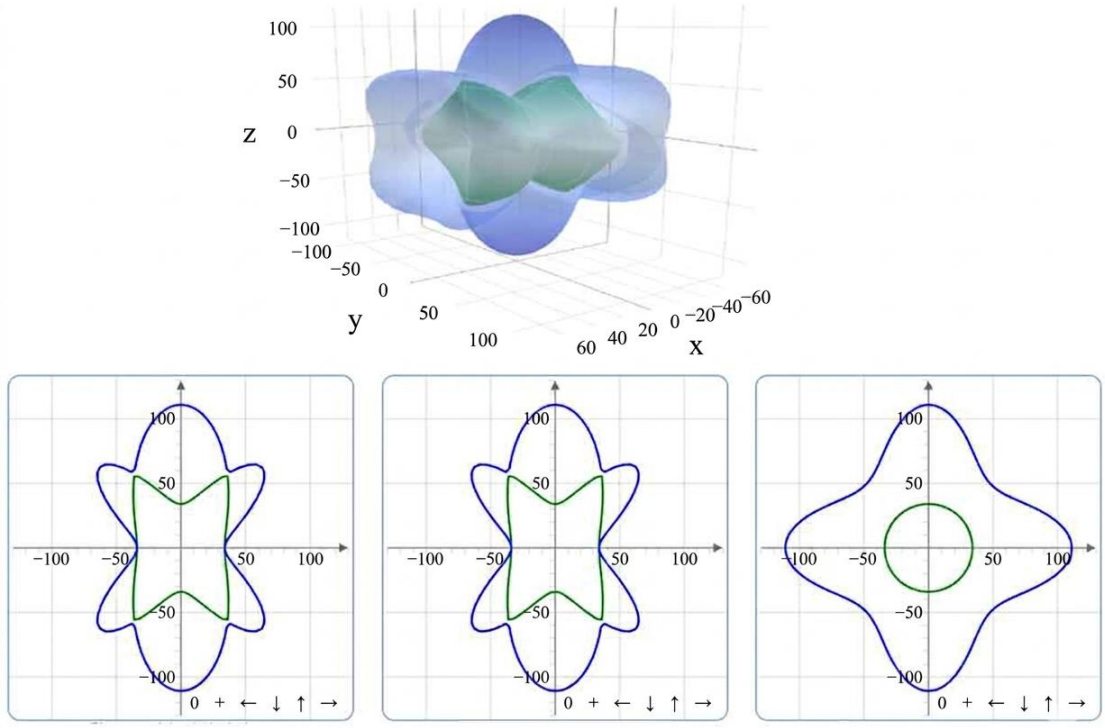


**Fig. 17 3-D variation (left) of the shear modulus G and its spatial dependence in various panes (right) corresponding to the $CaCuO_2$ compound is plotted using ELATE software**

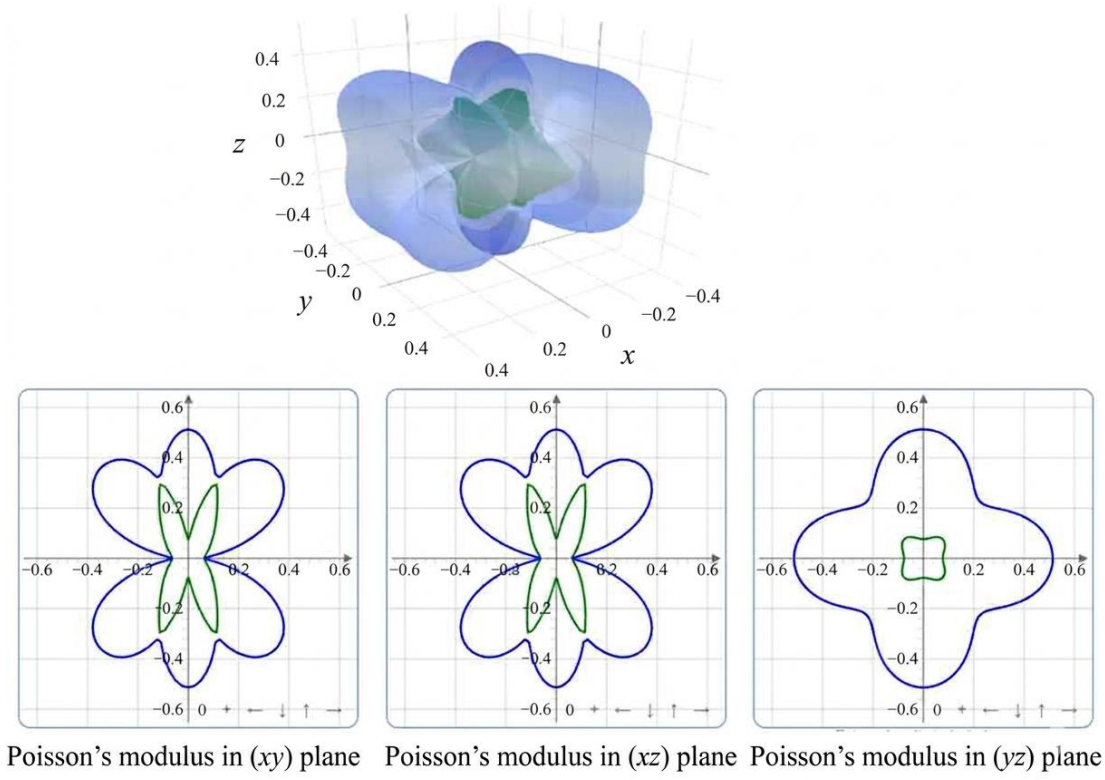


**Fig. 18 3-D variation (left) of the Poisson's ratio $n$ & its spatial dependence in various panes (right) corresponding to the $CaCuO_2$ compound is plotted using ELATE software**

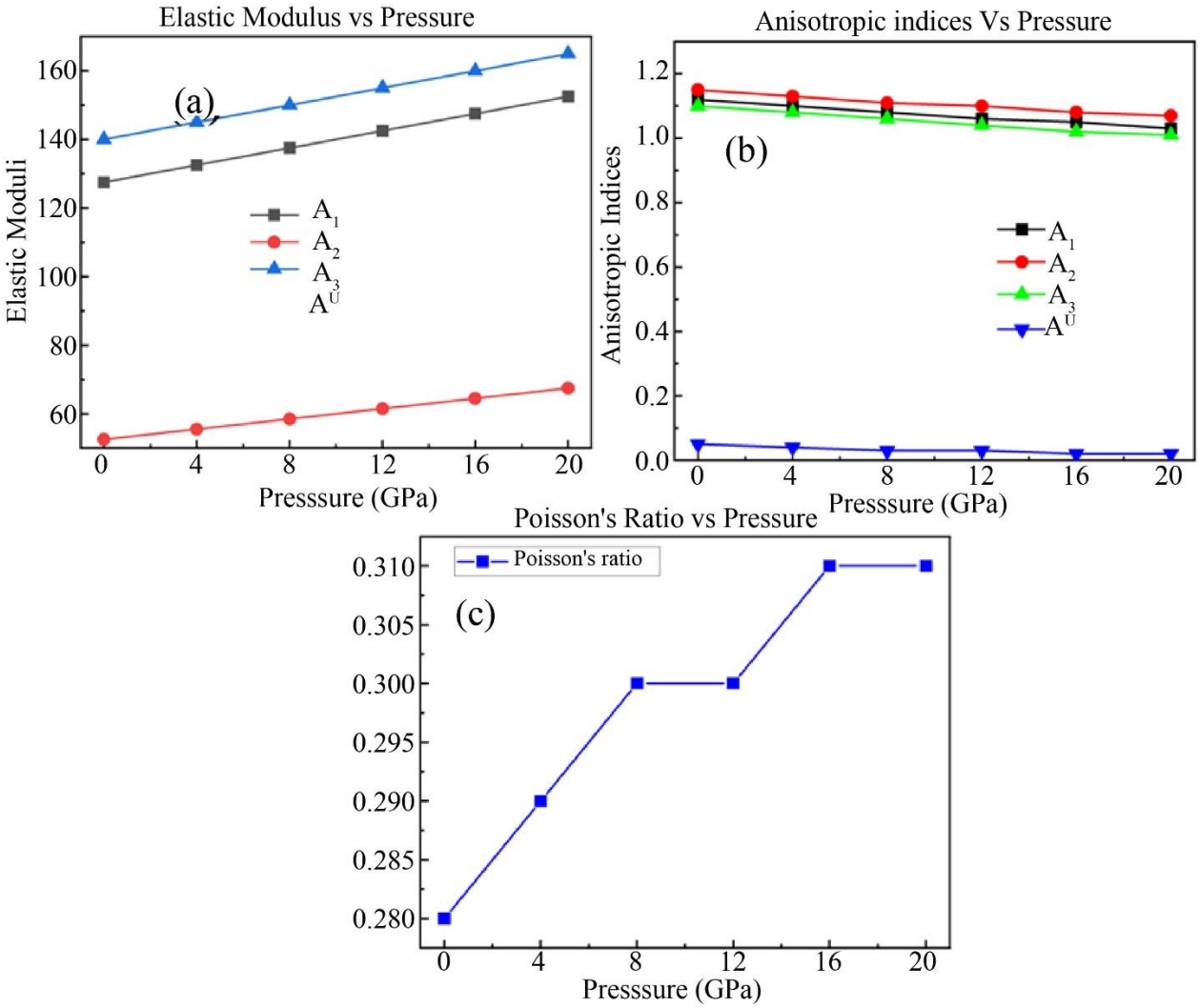


**Fig. 19 Graphical representation of (a) elastic modulus, (b) anisotropic indices, and (c) Poisson's ratio vs pressure for the $CaCuO_2$ crystal.**

Elastic moduli variation with applied pressure is shown in Figure 19(a): B, G, and Y are presented. The stress dependence of the bulk modulus (B) and Young's modulus (Y) is of the same character, which means there is a greater stiffening against volume and shape changes. Just as the shear modulus (G) gradually increases, so does rigidity under compression.

The overall trend indicates that the material will become stiffer with increasing pressure, which is important for understanding its mechanics under high pressure. The anisotropic indices (A1, A2, A3, and $A^U$) versus pressure are given in Figure 19(b). Increasing pressure leads to a decreasing trend in the anisotropic indices ($A_1$, $A_2$, $A_3$ & $A^U$), implying a decrease in mechanical anisotropy.

It indicates isotropic behavior during uniaxial compression, which can affect mechanical performance and failure mechanisms. Ongoing work suggests that the universal Anisotropy Index ($A^U$), which remains close to zero, further indicates that the material is near isotropic under an elevated force. In Figure 19(c), the change of v with pressure is shown. Poisson's ratio increases to a stable value at higher pressures. It indicates the potential for lateral expansion under axial compression. The increase in Poisson's ratio affects the mechanical and vibrational properties with pressure.

**Table 6. Variation of Pressure-induced (BV, BR, and B), i.e., the Bulk Moduli, (GV, GR, and G) i.e., the Shear Moduli, Y i.e. the Young's Modulus, Poisson's Ratio (v), Shear & Universal Anisotropy Indices ($A_1$, $A_2$, $A_3$ & $A^U$) & (B/G) i.e. the Pugh Ratio of $CaCuO_2$.**

| P (GPa) | Bv | $B^R$ | B | Gv | $G^R$ | G | Y |
|---|---|---|---|---|---|---|---|
| 0 | 130 | 125 | 127.5 | 55 | 50 | 52.5 | 140 |
| 4 | 135 | 130 | 132.5 | 58 | 53 | 55.5 | 145 |
| 8 | 140 | 135 | 137.5 | 61 | 56 | 58.5 | 150 |
| 12 | 145 | 140 | 142.5 | 64 | 59 | 61.5 | 155 |
| 16 | 150 | 145 | 147.5 | 67 | 62 | 64.5 | 160 |
| 20 | 155 | 150 | 152.5 | 70 | 65 | 67.5 | 165 |

| P (GPa) | ν | $A_1$ | $A_2$ | $A_3$ | $A^U$ | B/G |
|---|---|---|---|---|---|---|
| 0 | 0.28 | 1.12 | 1.15 | 1.10 | 0.05 | 2.43 |
| 4 | 0.29 | 1.10 | 1.13 | 1.08 | 0.04 | 2.39 |
| 8 | 0.30 | 1.08 | 1.11 | 1.06 | 0.03 | 2.35 |
| 12 | 0.30 | 1.06 | 1.10 | 1.04 | 0.03 | 2.32 |
| 16 | 0.31 | 1.05 | 1.08 | 1.02 | 0.02 | 2.29 |
| 20 | 0.31 | 1.03 | 1.07 | 1.01 | 0.02 | 2.26 |

## 4. Conclusion

The study analyzed the electronic, structural, and mechanical behavior of $CaCuO_2$ by DFT calculations. The $CaCuO_2$ possesses the tetragonal P4/mmm space group, as found from the structural study. It is influenced by the layered Cu-O structure surrounding a central Ca atom. The metallic Nature of $CaCuO_2$ is inferred from the band structure calculation by the presence of free charge carriers. The contribution of Cu(3d) & O(2p) orbitals to the Fermi-level electronic states is studied through DOS analysis. The anisotropic compression of the lattice structure is found from 0 to 20 GPa applied pressure. It also resulted in increased mechanical stiffness and stability. The increased Poisson's ratio indicates less compressibility under axial stress in $CaCuO_2$. The observed shift and relative intensity differences are studied through TDOS and PDOS. The mechanical stability of the material is confirmed by its increased elastic constants under pressure, making it suitable for high-pressure applications. The changes observed in elastic constants, Fermi surface topology, and Density of states are favorable for electron-phonon interactions, which are essential for superconducting Nature. The superconducting state of $CaCuO_2$ is also further studied through phonon dispersion and electron-phonon coupling interactions. The present study investigated the electronic, structural, and mechanical properties of $CaCuO_2$ under different pressure conditions. The outputs from different analyses showed the potential applications of $CaCuO_2$ in superconducting and high-pressure electronic devices due to its tunable electronic properties.

## Data availability

Data will be provided upon reasonable request.

## Declarations

***Ethics approval and consent to participate***

The paper is not currently being considered for publication elsewhere.

## Consent to publication:

Not applicable.

## Competing interests:

The authors have no relevant financial or non-financial interests to disclose. The authors declare: no conflict of interest.

## References


[1] Warren E. Pickett, "Electronic Structure of the High-Temperature Oxide Superconductors," *Reviews of Modern Physics*, vol. 61, no. 2, 1989. [CrossRef] [Google Scholar] [Publisher Link]

[2] A. Schilling et al., "Superconductivity above 130 K in the Hg–Ba–Ca–Cu–O System, *Nature*, vol. 363, no. 6424, pp. 56-58, 1993. [CrossRef] [Google Scholar] [Publisher Link]

[3] Hua Wu et al., "The Electronic Structure of $CaCuO_2$ and $SrCuO_2$," *Journal of Physics: Condensed Matter*, vol. 11, no. 24, pp. 4637-4646, 1999. [CrossRef] [Google Scholar] [Publisher Link]

[4] L.F. Mattheiss, "Electronic band Properties and Superconductivity in $La_{2-y}X_yCuO_4$," *Physical Review Letters*, vol. 58, no. 10, 1987. [CrossRef] [Google Scholar] [Publisher Link]

[5] J.P. Perdew, and Alex Zunger, "Self-Interaction Correction to Density-Functional Approximations for Many-Electron Systems," *Physical Review B*, vol. 23, no. 10, pp. 5048-5079, 1981. [CrossRef] [Google Scholar] [Publisher Link]

[6] John P. Perdew, Kieron Burke, and Matthias Ernzerhof, "Generalized Gradient Approximation made Simple," *Physical Review Letters*, vol. 77, no. 18, pp. 3865-3868, 1996. [CrossRef] [Google Scholar] [Publisher Link]

[7] M.T. Czyżyk, and G.A. Sawatzky, "Local-Density Functional and On-Site Correlations: The Electronic Structure of $La_2CuO_4$ and $LaCuO_3$," *Physical Review Letters*, vol. 49, no. 20, 1994. [CrossRef] [Google Scholar] [Publisher Link]

[8] Lucas K. Wagner, and Peter Abbamonte, "Effect of Electron Correlation on the Electronic Structure and Spin-Lattice Coupling of high-*Tc* Cuprates: Quantum Monte Carlo Calculations, *Physical Review B*, vol. 90, no. 12, pp. 1-8, 2014. [CrossRef] [Google Scholar] [Publisher Link]

[9] Paolo Giannozzi et al., "QUANTUM ESPRESSO: A Modular and Open-Source Software Project for Quantum Simulations of Materials," *Journal of Physics: Condensed Matter*, vol. 21, no. 39, pp. 1-36, 2009. [CrossRef] [Google Scholar] [Publisher Link]

[10] P. Giannozzi et al, "Advanced Capabilities for Materials Modelling with QUANTUM ESPRESSO," *Journal of Physics: Condensed Matter*, vol. 29, no. 46, pp. 1-68, 2017. [CrossRef] [Google Scholar] [Publisher Link]

[11] Paolo Giannozzi et al, "Quantum ESPRESSO Toward the Exascale," *The Journal of Chemical Physics*, vol. 152, no. 15, 2020. [CrossRef] [Google Scholar] [Publisher Link]

[12] M.D. Segall et al., "First-Principles Simulation: Ideas, Illustrations and the CASTEP Code," *Journal of Physics: Condensed Matter*, vol. 14, no. 11, pp. 2717-2744, 2002. [CrossRef] [Google Scholar] [Publisher Link]

[13] E. Stellino et al., "On the Role of Strain- and Doping-Induced Disorder in Epitaxial $CaCuO_2$ Films: Lattice and Spin Dynamics in Light Scattering Response," *Journal of Applied Physics*, vol. 137, no. 18, pp. 1-8, 2025. [CrossRef] [Google Scholar] [Publisher Link]

[14] David J. Abramovitch et al., "Electron-Phonon Coupling in Correlated Metals: A Dynamical Mean-Field Theory Study," *Physical Review B*, vol. 112, no. 7, pp. 1-16, 2025. [CrossRef] [Google Scholar] [Publisher Link]

[15] Jonathan Karp et al., "Many-Body Electronic Structure of $NdNiO_2$ and CaCuO," *Physical Review X*, vol. 10, no. 2, pp. 1-11, 2020. [CrossRef] [Google Scholar] [Publisher Link]

[16] Chun Yu Chow, William A. Wheeler, and Lucas K. Wagner, "Capturing Spin Fluctuations in $CaCuO_2$: *Ab initio* Quantum Monte Carlo Calculations with Multideterminant Wave Functions," *Physical Review B*, vol. 110, no. 23, pp. 1-8, 2024. [CrossRef] [Google Scholar] [Publisher Link]

[17] Jonathan Karp, Alexander Hampel, and Andrew J. Millis, "Superconductivity and Antiferromagnetism in $NdNiO_2$ and $CaCuO_2$: A Cluster DMFT Study," *Physical Review B*, vol. 105, no. 20, pp. 1-11, 2022. [CrossRef] [Google Scholar] [Publisher Link]

[18] Bal K. Agrawal, and Savitri Agrawal, "Structural, Dynamical, and Electronic Properties of $CaCuO_2$," *Physical Review B*, vol. 48, no. 9, 1993. [CrossRef] [Google Scholar] [Publisher Link]

[19] Andrey L. Kutepov, "Electronic Structure of LaNiO2 and $CaCuO_2$ from a Self-Consistent Vertex-Corrected *GW* Approach," *Physical Review B*, vol. 104, no. 8, pp. 1-12, 2021. [CrossRef] [Google Scholar] [Publisher Link]

[20] G. Kotliar et al., "Electronic Structure Calculations with Dynamical Mean-Field Theory," *Reviews of Modern Physics*, vol. 78, no. 3, pp. 865-951, 2006. [CrossRef] [Google Scholar] [Publisher Link]

[21] K. Held et al., "Realistic Investigations of Correlated Electron Systems with LDA+DMFT," *Physica Status Solidi (b)*, vol. 243, no. 11, pp. 2599-2631, 2006. [CrossRef] [Google Scholar] [Publisher Link]

[22] H. Park, K. Haule, and G. Kotliar, "Cluster Dynamical mean Field Theory of the Mott Transition," *Physical Review Letters*, vol. 101, no. 18, pp. 1-5, 2008. [CrossRef] [Google Scholar] [Publisher Link]

[23] H. Azhan et al., "Superconducting Properties of Ag and Sb Substitution on Low-Density $YBa_2Cu_3O_\delta$ Superconductor," *Journal of Superconductivity and Novel Magnetism*, vol. 26, no. 4, pp. 931-935, 2012. [CrossRef] [Google Scholar] [Publisher Link]

[24] L. Sharifzadegan, and H. Sedghi, "Investigation of Sm Substitution on Structural and Superconducting Properties of $Y1Ba_{2-x}SmxCu_3O_{7-\delta}$ Superconductors," *Physica C: Superconductivity and its Applications*, vol. 550, pp. 7-9, 2018. [CrossRef] [Google Scholar] [Publisher Link]

[25] Stefano Baroni et al., "Phonons and Related Crystal Properties from Density-Functional Perturbation Theory," *Reviews of Modern Physics*, vol. 73, no. 2, pp. 1-52, 2001. [CrossRef] [Google Scholar] [Publisher Link]

[26] Romain Gaillac, Pluton Pullumbi, and François-Xavier Coudert, "ELATE: An Open-Source Online Application for Analysis and Visualization of Elastic tensors," *Journal of Physics: Condensed Matter*, vol. 28, no. 27, pp. 1-10, 2016. [CrossRef] [Google Scholar] [Publisher Link]

[27] M. Momma, and F. Izumi, "VESTA a Three-Dimensional Visualization System for Electronic and Structural Analysis," *Journal of Applied Crystallography*, vol. 41, no. 3, pp. 653-658, 2008. [CrossRef] [Google Scholar] [Publisher Link]

[28] M. Momma, and F. Izumi, "VESTA 3 for Three-Dimensional Visualization of Crystal, Volumetric and Morphology Data," *Journal of Applied Crystallography*, vol. 44, no. 6, pp. 1272-1276, 2011. [CrossRef] [Google Scholar] [Publisher Link]

[29] A. Floris et al., "Vibrational Properties of MnO and NiO from DFT+*U*-based Density Functional Perturbation Theory," *Physical Review B*, vol. 84, no. 16, pp. 1-4, 2011. [CrossRef] [Google Scholar] [Publisher Link]

[30] Guido Petretto et al., "High-Throughput Density-Functional Perturbation Theory Phonons for Inorganic Materials," *Scientific Data*, vol. 5, no. 1, pp. 1-12, 2018. [CrossRef] [Google Scholar] [Publisher Link]

[31] Vladimir I. Anisimov, Jan Zaanen, and Ole K. Andersen, "Band Theory and Mott Insulators: Hubbard *U* Instead of Stoner *I*," *Physical Review B*, vol. 44, no. 3, 1991. [CrossRef] [Google Scholar] [Publisher Link]

[32] G. Kresse, "Efficient Iterative Schemes for ab Initio Total-Energy Calculations using a Plane-Wave basis Set," *Physical Review B*, vol. 54, no. 16, pp. 11169-11186, 1996. [CrossRef] [Google Scholar] [Publisher Link]

[33] P.E. Blöchl, "Projector Augmented-Wave Method," *Physical Review B*, vol. 50, no. 24, pp. 17953-17979, 1994. [CrossRef] [Google Scholar] [Publisher Link]

[34] Matteo Cococcioni, and Stefano de Gironcoli, "Linear Response Approach to the Calculation of the Effective Interaction Parameters in the LDA+U Method," *Physical Review B*, vol. 71, no. 3, pp. 1-18, 2005. [CrossRef] [Google Scholar] [Publisher Link]

[35] Nicola Marzari, and David Vanderbilt, "Maximally Localized Generalized Wannier Functions for Composite Energy Bands," *Physical Review B*, vol. 56, no. 20, pp. 1-22, 1997. [CrossRef] [Google Scholar] [Publisher Link]

[36] P. Hohenberg, and W. Khon, "Inhomogeneous Electron Gas," *Physical Review Journals Archive*, vol. 136, no. 3B, pp. B864-B871,1964. [CrossRef] [Google Scholar] [Publisher Link]

[37] W. Kohn, and L.J. Sham, "Self-Consistent Equations Including Exchange and Correlation Effects," *Physical Review Journals Archive*, vol. 140, no. 4A, pp. A1133-A1138,1965. [CrossRef] [Google Scholar] [Publisher Link]

[38] Ahmad Yazdani, and Behrad Barakati, "A First-Principles Study on Electronic Structure and Crustal Field Effect of Layered $La_2CuO_4$ as Composed of $CuO_2$ and $LaO_2$ Monolayers," *Physica E: Low-Dimensional Systems and Nanostructures*, vol. 125, 2021. [CrossRef] [Google Scholar] [Publisher Link]

[39] P.W. Anderson et al., "Resonating-Valence-Bond Theory of Phase Transitions and Superconductivity in $La_2CuO_4$-based Compounds," *Physical Review Letters*, vol. 58, no. 26, 1987. [CrossRef] [Google Scholar] [Publisher Link]

[40] P.S. Häfliger et al., "Quantum and Thermal Ionic Motion, Oxygen Isotope Effect and Superexchange Distribution in $La_2CuO_4$," *Physical Review B*, vol. 89, no. 8, pp. 1-13, 2014. [CrossRef] [Google Scholar] [Publisher Link]

[41] F. Essenberger et al., "Superconducting Pairing Mediated by Spin Fluctuations from First Principles," *Physical Review B*, vol. 90, no. 21, pp. 1-13, 2014. [CrossRef] [Google Scholar] [Publisher Link]

[42] Simon Pesant, and Michel Côté, "DFT + *U* Study of Magnetic Order in Doped $La_2CuO_4$ Crystals," *Physical Review B*, vol. 84, no. 8, pp. 1-7, 2011. [CrossRef] [Google Scholar] [Publisher Link]

[43] G.P. Malik, and P.S. Varma, "A Study of Superconducting $La_2CuO_4$ via Generalized BCS Incorporating Chemical Potential," *World Journal of Condensed Matter Physics*, vol. 5, pp. 148-159, 2015. [CrossRef] [Google Scholar] [Publisher Link]

[44] Shin-ichi Uchida et al., "Electric and Magnetic Properties of $La_2CuO_4$," *Japanese Journal of Applied Physics*, vol. 26, no. 4A, 1987. [CrossRef] [Google Scholar] [Publisher Link]

[45] J.G. Bednorz, and K.A. Müller, "Possible High $T_c$ Superconductivity in Ba-La-Cu-O System," *Zeitschrift für Physik B Condensed Matter*, vol. 64, no. 2, pp. 189-193, 1986. [CrossRef] [Google Scholar] [Publisher Link]

[46] H.k. Müller-Buschbaum, and M.W. Wollschläger, "On Oxocuprates VII, on the Crystal Structure of $Nd_2CuO_4$," *Journal of Inorganic and General Chemistry*, vol. 414, no. 1, pp. 76-80, 1975. [CrossRef] [Google Scholar] [Publisher Link]

[47] S.I. Seok, and D.S. Park, "Electrical Characterization of Co-Doped $La_2CuO_{4+\delta}$ at Elevated Temperature," *Materials Research Bulletin*, vol. 34, no. 2, pp. 315-325, 1999. [CrossRef] [Google Scholar] [Publisher Link]

[48] Hiroyuki Yasuda, Noritaka Mizuno, and Makoto Misono, "Role of Valency of Copper in the Direct Decomposition of Nitrogen Monoxide Over Well Characterized $La_{2x}A'_xCu_{1-y}B'_yO_4$," *Journal of the Chemical Society, Chemical Communications*, vol. 16, pp. 1094-1096, 1990. [CrossRef] [Google Scholar] [Publisher Link]

[49] Huihuang Jiang, Zhijie Yang, and Feng Zhang, "Preparation, Characterization and Electrochemical Properties of $La_2CuO_4$@Au as a Novel Bifunctional Oxygen Electrode," *International Journal of Electrochemical Science*, vol. 15, no. 10, pp. 9933-9939, 2020. [CrossRef] [Google Scholar] [Publisher Link]

[50] David Sénéchal et al., "Competition between Antiferromagnetism and Superconductivity in High-$T_c$ Cuprates," *Physical Review Letters*, vol. 94, no. 15, pp. 1-5, 2005. [CrossRef] [Google Scholar] [Publisher Link]

[51] Michael J. Pitcher et al., "Structure and Superconductivity of LiFeAs," *Chemical Communications*, no. 45, pp. 5918-5920, 2008. [CrossRef] [Google Scholar] [Publisher Link]

[52] Y. Krockenberger et al., "Superconductivity Phase Diagrams for the Electron-Doped Cuprates $R_{2-x}$ $Ce_x$ Cu $O_4$ ($R$=La, Pr, Nd, Sm, and Eu)," *Physical Review B*, vol. 77, no. 6, pp. 1-5, 2008. [CrossRef] [Google Scholar] [Publisher Link]

[53] Nicola Poccia et al., "Optimum Inhomogeneity of Local Lattice Distortions in $La_2CuO_{4+y}$," *PNAS*, vol. 109, no. 39, pp. 15685-15690, 2012. [CrossRef] [Google Scholar] [Publisher Link]

[54] R. Hord et al., "Oxygen Stoichiometry of Low-Temperature Synthesized Metastable $T'$-$La_2CuO_4$," *Superconductor Science and Technology*, vol. 26, no. 10, 2013. [CrossRef] [Google Scholar] [Publisher Link]

[55] S.W. Cheong, J.D. Thompson, and Z. Fisk, "*Properties of $La_2CuO_4$ and Related Compounds*," *Physica C: Superconductivity*, vol. 158, no. 1-2, pp. 109-126, 1989. [CrossRef] [Google Scholar] [Publisher Link]

[56] M.K. Crawford et al., "Oxygen Isotope Effect and Structural Phase Transitions in $La_2CuO_4$-based Superconductors," *Science*, vol. 250, no. 4986, pp. 1390-1394, 1990.

[57] J.P. Attfield, A.L. Kharlanov, and J.A. McAllister, "Cation Effects in Doped $La_2CuO_4$superconductors, *Nature*, vol. 394, pp. 157-159, 1998. [CrossRef] [Google Scholar] [Publisher Link]

[58] Eun-Mi Choi et al., "Magnetic Signatures of 120 K Superconductivity at Interfaces in $La_2CuO_{4+\delta}$," *Nanoscale*, vol. 12, no. 5, pp. 3157-3165, 2020. [CrossRef] [Google Scholar] [Publisher Link]

[59] R. Hord et al., "Enhanced two Dimensional Behavior of Metastable T′-$La_2CuO_4$, the Parent Compound of Electron-Doped Cuprate Superconductors," *Physical Review B*, vol. 82, no. 18, pp. 1-4, 2010. [CrossRef] [Google Scholar] [Publisher Link]

[60] N.M. Plakida, and V.S. Oudovenko, "Theory of High-Temperature Superconductivity in Cuprates," *Journal of Superconductivity and Novel Magnetism*, vol. 29, no. 4, pp. 1037-1042, 2016. [CrossRef] [Google Scholar] [Publisher Link]

[61] Tomoo Katsura, and Yoshinori Tange, "A Simple Derivation of the Birch-Murnaghan Equations of State (EOSs) and Comparison with EOSs Derived from Other Definitions of Finite Strain," *Minerals*, vol. 9, no. 12, pp. 1-19, 2019. [CrossRef] [Google Scholar] [Publisher Link]

[62] V.I. Anisimov, D. Bukhvalov, and T.M. Rice, "Electronic Structure of Possible Nickelate Analogs to the Cuprates," *Physical Review B*, vol. 59, no. 12, pp. 7901-7906, 1999. [CrossRef] [Google Scholar] [Publisher Link]

[63] Z.H. Liu et al., "Oribtal Characters and Electronic Correlations in $KCo_2Se_2$," *Journal of Physics: Condensed Matter*, vol. 27, no. 29, 2015. [CrossRef] [Google Scholar] [Publisher Link]

[64] Neil C. Hyatt et al., "Structure-Compressibility Relationships in Layered Cuprate Materials," *Physical Review B*, vol. 65, no. 1, 2001. [CrossRef] [Google Scholar] [Publisher Link]

[65] E. Liarokapis et al., "Pressure Induced Lattice Instability and Phase Separation in the Cuprates," *Journal of Physics and Chemistry of Solids*, vol. 71, no. 8, pp. 1084-1087, 2010. [CrossRef] [Google Scholar] [Publisher Link]

[66] O.K. Andersen et al., "LDA Energy Bands, Low-Energy Hamiltonians, t′, t″, t⊥(k) and *J*⊥," *Journal of Physics and Chemistry of Solids*, vol. 56, no. 12, pp. 1573-1591, 1995. [CrossRef] [Google Scholar] [Publisher Link]

[67] Yoshikazu Mizuguchi et al., "Superconductivity at 27 K in Tetragonal FeSe Under High Pressure," *Applied Physics Letters*, vol. 93, no. 15, 2008. [CrossRef] [Google Scholar] [Publisher Link]

[68] Joshua H. Tapp et al., "LiFeAs: An Intrinsic FeAs-based Superconductor with $T_c$=18K," *Physical Review B*, vol. 78, no. 6, pp. 1-4, 2008. [CrossRef] [Google Scholar] [Publisher Link]

[69] Damian Rybicki et al., "Perspective on the Phase Diagram of Cuprate High-Temperature Superconductors," *Nature Communications*, vol. 7, no. 1, pp. 1-6, 2016. [CrossRef] [Google Scholar] [Publisher Link]

[70] Tetsuro Saito, Seiichiro Onari, and Hiroshi Kontani, "Orbital Fluctuation Theory in Iron Pnictides: Effects of As-Fe-As Bond Angle, Isotope Substitution and $Z^2$-Orbital Pocket on Superconductivity," *Physical Review B*, vol. 82, no. 14, pp. 1-11, 2010. [CrossRef] [Google Scholar] [Publisher Link]

[71] L. Ortenzi et al., "Accounting for Spin Fluctuations Beyond Local Spin Density Approximation in the Density Functional Theory," *Physical Review B*, vol. 86, no. 6, pp. 1-7, 2012. [CrossRef] [Google Scholar] [Publisher Link]

[72] Christian Platt, Ronny Thomale, and Werner Hanke, "Superconducting State of the Iron Pnictide LiFeAs: A Combined Density-Functional and Functional-Renormalization-Group Study," *Physical Review B*, vol. 84, no. 23, 2011. [CrossRef] [Google Scholar] [Publisher Link]

[73] Elliot Snider et al., "Retracted Article: Room-Temperature Superconductivity in a Carbonaceous Sulfur Hydride," *Nature*, vol. 586, no. 7829, pp. 373-377, 2020. [CrossRef] [Google Scholar] [Publisher Link]

[74] B.P.P. Mallett et al., "Dielectric Versus Magnetic Pairing Mechanisms in High-Temperature Cuprate Superconductors Investigated using Raman Scattering," *Physical Review Letters*, vol. 111, no. 23, pp. 1-9, 2013. [CrossRef] [Google Scholar] [Publisher Link]

[75] J. Clark Stewart et al., "First Principles Methods using CASTEP," *Zeitschrift für Kristallographie*, pp. 567-570, 2005. [CrossRef] [Google Scholar] [Publisher Link]